Photopatternable hydroxide ion electrolyte for solid-state micro-supercapacitors

Christopher Choi, Kevin Robert, Grace Whang, Pascal Roussel, Christophe Lethien, Bruce Dunn

To cite this version:

Christopher Choi, Kevin Robert, Grace Whang, Pascal Roussel, Christophe Lethien, et al.. Photopatternable hydroxide ion electrolyte for solid-state micro-supercapacitors. Joule, 2021, 5 (9), pp.2466-2478. ⟨10.1016/j.joule.2021.07.003⟩. ⟨hal-03501780⟩

HAL Id: hal-03501780

https://hal.science/hal-03501780v1

Submitted on 22 Apr 2022

Photopatternable hydroxide ion electrolyte for solid-state micro-supercapacitors

Christopher Choi[†], Kevin Robert[§,‖], Grace Whang[†], Pascal Roussel[¥], Christophe Lethien[§,‖,#,*] and Bruce Dunn[†,+,*]

Affiliations:

† Department of Materials Science and Engineering, University of California, Los Angeles, CA 90095,
USA.

§ Institut d'Electronique, de Microélectronique et de Nanotechnologies, Université de Lille, CNRS, 8 Centrale Lille, Université Polytechnique Hauts-de-France, UMR 8520 - IEMN, F-59000 Lille, France

‖ Réseau sur le Stockage Electrochimique de l'Energie (RS2E), CNRS FR 3459, 33 rue Saint Leu, 80039 Amiens Cedex, Fr

[¥] Unité de Catalyse et de Chimie du Solide (UCCS), Université de Lille, CNRS, Centrale Lille, Université d'Artois, UMR 8181 – UCCS, F-59000 Lille, France

Institut Universitaire de France (IUF)

\+ Lead Contact

✉: christophe.lethien@univ-lille.fr, bdunn@ucla.edu

Keywords

Solid electrolytes, hydroxide-ion electrolytes, photopatternable electrolytes, on-chip energy storage, micro-supercapacitors

Summary

Electrochemical energy storage (EES) devices that provide high power and energy for micropower systems are considered to be essential for developing micro/nano electronics, such as nanorobotics, environmental sensors, and connected smart electronics. One promising research direction in this field has been to develop

on-chip EES whose length scales integrate with those of miniaturized electronic devices. In the work described here, we provide the first report of a hydroxide ion conducting solid electrolyte which can be patterned using standard lithography. By combining a negative photoresist with a polymerizable ionic liquid, we obtain a thermally and dimensionally stable, hydroxide ion conducting solid electrolyte with a conductivity of 10 mS cm^{-1}. Patterning the solid electrolyte directly on interdigitated vanadium nitride (VN) electrodes enables a scalable fabrication approach for producing high resolution, solid-state VN micro-supercapacitors (MSC) in both single and multiple devices. Individual solid-state MSC devices exhibit better areal energy and power densities compared to previously reported solid-state MSC systems while tandem VN MSC devices demonstrated the ability to increase the cell working voltage and total current output. These results effectively extend the field of on-chip micro-supercapacitors into the important direction of integrated high-energy and high-power solid-state EES devices for powering IoT technology.

Introduction

Advances in electrochemical energy storage (EES) technology have changed the landscape of the portable electronics industry and the electric vehicle market in the past decade and are on the same track for enabling the 'Internet of Things' (IoT).[1] A robust, high-energy and high-power micropower system is a key technology for the future development of micro/nano electronics, such as nanorobotics, microelectromechanical systems (MEMS), environmental sensors, and connected smart electronics.[2,3] However, the power sources for these devices often become the limitation in achieving the small formfactor required by miniaturized electronics because energy-storage components scale down poorly in size. It is well known that miniaturization of electrochemical energy storage (EES) system devices such as batteries and capacitors have lagged far behind Moore's Law and that improvements of only about 10%/year have been achieved.[4] A brief overview of miniaturized EES that use various fabrication methods is presented in the SI and summarized in Table S1. Of particular interest for the current research is the development of integrated on-chip EES to power miniaturized electronic devices. Such a technology holds significant promise towards enabling the IoT and further enhancing the distribution and utilization of sustainable energy. To achieve this goal, however, there needs to be an appropriate chemistry where EES components, i.e. the anode, cathode, and solid electrolyte, can be formed and defined spatially through the very techniques that are utilized in achieving high-resolution patterns in the semiconductor industry.[5,6]

In recent years, there have been substantial efforts at fabricating EES devices using semiconductor processing fabrication methods. This research includes on-chip micro-supercapacitors (MSC)[7–10] and multi-dimensional batteries.[5,11–13] Some devices have demonstrated areal energy densities (> 1 mWh cm^{-2}) or power densities (> 5 mW cm^{-2}) that are comparable to those of bulk-scale EES systems. However, these micropower sources use liquid electrolytes which are not compatible with on-chip integration because of the inability to spatially confine a liquid. There is, therefore, a critical need to develop solid electrolyte materials which would enable the fabrication of micropower sources using semiconductor processing methods. Typical solid electrolytes for miniaturized MSC devices consist of an ionic salt solvated in polymeric or inorganic solid host materials. The most popular solid electrolytes being explored for supercapacitors use aqueous electrolytes embedded in polymer hydrogels such as poly(vinyl alcohol) (PVA), poly(ethylene oxide) (PEO), and poly(acrylic acid) (PAA).[14–17] A representative system is KOH in PVA, which exhibits an ionic conductivity exceeding 10^{-2} S cm^{-1} at room temperature. Ionogel electrolytes, based on the incorporation of an ionic liquid such as 1-ethyl-3-methylimidazolium bis(trifluoromethylsulfonyl)imide [EMIM][TFSI] encapsulated in SiO_2 or polyvinylidene fluoride, constitutes another class of solid electrolyte that is used in supercapacitors.[18] This nonaqueous solid electrolyte exhibits an electrochemical window up to 2.5 V in MSCs, although its ionic conductivity at ambient temperatures (10^{-3} to 10^{-4} S cm^{-1}) is lower than aqueous systems due to slow diffusivity of the bulky ions.[19] Both of these systems represent gel-type electrolytes whose utilization in advanced devices is restricted by several concerns including poor mechanical integrity and fabrication difficulties which limit their integration with high resolution devices.[20,21]

In this paper, we describe the development of a hydroxide-conducting photopatternable solid electrolyte that possesses a high room temperature ionic conductivity of 10 mS cm^{-1} along with excellent thermal stability and mechanical integrity. This material represents one of the very few photopatternable solid electrolytes reported to date and, to the best of our knowledge, is the first one to exhibit hydroxide ion conduction. This solid-state electrolyte, and especially its ability to be photopatterned, enables interdigitated MSC to be fully fabricated by semiconductor processing methods. We demonstrate the application of the hydroxide-conducting photopatternable solid electrolyte by integrating it with VN interdigitated electrodes, leading to the fabrication of high-resolution, high performance solid-state VN MSC devices. In addition to demonstrating individual MSC devices, we characterize tandem device architectures which lead to increased cell voltages and total currents beyond what is available with individual devices.

Results and Discussion

Our approach to creating photopatternable solid electrolyte materials involves modifying the chemistry of commercial SU-8 photoresists to achieve ion transport without compromising its photopatterning functionality. We previously demonstrated this general methodology enabling the development of lithiumion conducting photopatterned electrolytes with sub-100 μm resolution.[6] In the research reported here, the particular challenge in achieving hydroxide-ion conduction is the hydrophobic nature of the SU-8 photoresist. Our synthesis strategy for preparing the photopatternable hydroxide-conducting solid electrolyte involved two steps. First, the cationic polymerizable 1-Allyl-3-methylimidazolium bis(trifluoromethylsulfonyl)imide [AMIM][TFSI] was grafted onto the SU-8 polymer matrix. This was followed by anion exchange to incorporate hydroxides (Figure 1a, S1). The resulting electrolyte system consists of the SU-8 host material that provides the photopatterning capability while hydroxides in the polymerizable ionic liquid phase provide the charge-carrying hydroxide ions required for the VN redox process (Figure 1b). Ionic liquid [AMIM][TFSI] grafted SU-8 polymer was successfully photopatterned using a photomask with cylindrical features 100 μm in diameter (Figure S1). This signifies that the photopatterned solid electrolyte material can be paired with any miniaturized EES systems that are 10 x 10 μm^2 in size. The photopatterned electrolyte was further characterized using energy-dispersive X-ray spectroscopy (EDS). The presence of ionic liquid constituents (sulfur and fluorine) in the photopatterned structure confirms that the photopatternable polymer matrix encapsulates the ionic liquid (Figure S1b). After the anion exchange process with hydroxides, only trace amounts of fluorine and sulfur were detected (Figure S1c).

The lithography-assisted crosslinking between polymerizable cations and SU-8 matrix was verified by analyzing Fourier transform infrared (FT-IR) spectra. The disappearance of the vinyl group at 1648 cm^{-1} (stretching vibration of C=C) upon polymerization indicates that vinyl groups are participating in the photopolymerization process (Figure S2a). The grafting of polymerizable ionic liquids was further confirmed by evaluating the solubility of the ionic liquid phase using an IL miscible solvent (i.e. acetone or ethanol). In general, for a given ionogel system, ionic liquids contained in the host network are readily soluble in certain solvent media.[18,21] However, it is evident in the infrared spectra in Figure S2b that polymerizable cations in the [AMIM][TFSI] ionic liquid are covalently bonded to the SU-8 matrix and are no longer soluble. Once grafting of the cation was confirmed, the mobile $TFSI^-$ anions were exchanged with OH^- in 1M KOH (aq.). The approximate concentration of hydroxide anions in [AMIM][OH]/SU-8 electrolyte is calculated to be 1.8M based on the total volume of the electrolyte with the assumption that $TFSI^-$ anions are fully substituted. The anion exchange process in the ionic liquid grafted SU-8 electrolyte was assessed by observing changes in the characteristic peaks (Figure 2a) ascribed to $TFSI^-$ anion (Table S2) and OH^- anion (3200-3400 cm^{-1}). It is also clear that the IR absorbance bands assigned to the imidazolium cation (752, 1432, 1464 cm^{-1}) are still present after the $TFSI^-$ anions are exchanged.

We validated the mobility of OH^- transport in the photopatternable [AMIM][OH]/SU-8 material by using it as a solid electrolyte which leads to charge storage in $NiCo_2O_4$. This transition metal oxide is well known for undergoing redox reactions with hydroxide anions through the following mechanisms[23,24]:

$$NiCo_2O_4 + \mathbf{OH^-} + H_2O \leftrightarrow NiOOH + 2CoOOH + e^- \qquad (1)$$

$$CoOOH + \mathbf{OH^-} \leftrightarrow CoO_2 + H_2O + e^- \qquad (2)$$

In this experiment, a 10 μm film of the [AMIM][OH]/SU-8 solid electrolyte was coated and polymerized on the $NiCo_2O_4$ electrode. The CV curves for this system were compared to those for the same $NiCo_2O_4$ material in 1M KOH (Figure S3). The similarity in redox potential, peak current response, and observed gravimetric capacities (89 vs 92 mAh g^{-1} at 10 mV s^{-1}) for $NiCo_2O_4$ samples tested in patternable solid electrolyte and 1M KOH control liquid electrolyte, confirms that hydroxide ion transport occurs in the patternable electrolyte. This observation was consistent over a range of sweep rates (1, 2, 5, 10 mV s^{-1}), suggesting that the [AMIM][OH]/SU-8 not only facilitates OH^- transport but also provides a coherent electrode/electrolyte interface. These attributes are among the most vital electrochemical features for solid electrolytes.

The thermal stability of the electrolyte was determined using thermogravimetric analysis (TGA) as shown in Figure 2b. In view of possible heating effects associated with high power operation, thermal stability of the electrolyte can be a potential concern. The photopatterned electrolyte is quite stable as it showed no appreciable weight loss to temperatures above 300 ^{o}C in the TG profile. In contrast, the unmodified SU-8 photoresist begins to undergo thermal decomposition below 200 ^{o}C (Figure S4a). One other feature of the solid-like behavior of [AMIM][OH]/SU-8 is that there is only a nominal change in the mechanical integrity after heat treatment (Figure S4b). The noticeable increase in thermal stability is attributed to the grafting of the thermally stable [AMIM]-based ionic liquid with the SU-8 matrix. Overall, the results showed excellent thermal stability with about 5 % weight loss by 320 ^{o}C.

The mechanical properties of the patternable solid electrolyte films were evaluated using nanoindentation measurements (Figure 2c). The mechanical integrity of the solid electrolyte is important for maintaining good contact with the electrodes and preventing electrical shorts. Prior to the ionic liquid grafting, the SU8 film demonstrates a high elastic modulus of 5.1 GPa. Upon incorporation of the polymerized ionic liquid phase, the elastic modulus value was reduced to 230 MPa. Nonetheless, the [AMIM][OH]/SU-8 ionogel electrolyte is far more rigid and dimensionally stable than that of the PVA/KOH gel electrolyte (3.75 MPa) and other gel electrolytes including PAA/KOH and polyacrylamide(PAM)/KOH.[25–27] To put this into perspective, the elastic modulus of 230 MPa (compressive) exceeds the 100 MPa elastic modulus requirement (tensile) identified for commercial Li-ion battery separators to possess sufficient mechanical integrity during battery manufacturing.[28,29] It is also important to reiterate that none of these other electrolytes have demonstrated photopatterning and thus, it is not possible to use these electrolytes to achieve the high spatial resolution that is required for on-chip integration.

One of the most favorable hydroxide-redox electrode materials for MSCs is VN. The material possesses high electronic conductivity (1.6×10^4 S cm^{-1}) with a high rate surface redox electrochemical response (Figure S5).[32] The preparation strategies and electrochemical characterization of interdigitated VN MSCs have been reported recently.[33] These MSC devices, however, were based on using a KOH aqueous electrolyte which is not compatible with on-chip integration because of the inability to spatially confine a liquid. The high-resolution photopatterning capability of [AMIM][OH]/SU-8 combined with interdigitated VN devices enables the integration of a solid-state MSC at the point-of-load and leads to in-series and/or in-parallel device configurations in a defined area.

The high electronic conductivity of the VN film allows it to be used as a blocking electrode in characterizing the impedance of the [AMIM][OH]/SU-8 ionogel electrolyte. Two- and three-electrode cells were used to compare the impedance of the ionogel electrolyte with that of 1M KOH. For the former, a 10 μm film of the ionogel electrolyte was patterned directly on VN electrodes. This thickness is comparable to the interlayer gap spacing distance used in the MSC interdigitated devices (*vide infra*). The Nyquist plot (Figure 3a, S8a) indicates that both electrolytes display a low series resistance with a low frequency capacitive tail. Despite the relatively low ionic conductivity of the patternable solid electrolyte compared to that of 1M KOH liquid electrolyte ($\sigma \sim 0.5\ S\ cm^{-1}$), the near-identical trend in impedance spectra highlights the effectiveness of high-resolution spatial control that can be achieved by [AMIM][OH]/SU-8 patterning. The room temperature ionic conductivity at 25 °C for the hydroxide conducting patternable solid electrolyte is calculated to be 10 mS cm^{-1} which represents a comparable or higher ionic conductivity than that of previously reported hydroxide-conducting electrolytes, such as PVA/KOH, PEO/KOH, and PAM/tetraethylammonium hydroxide.[34–37] Although PVA/KOH is the most widely used hydroxideconducting electrolyte for solid supercapacitors,[15,17] there has been only modest improvement in its electrochemical and physical properties since the adoption of PVA hydrogel chemistry. Additionally, the ionic conductivity of the [AMIM][OH]/SU-8 ionogel electrolyte is as much as 5 times higher than another polymer based ionogel, [EMIM][TFSI]/PVDF, which was incorporated in 3D MSCs with MnO_2 pseudocapacitive electrodes.[19,38] It is also interesting to note that the room temperature conductivity value for the hydroxide ion conducting electrolyte is comparable to that of conventional nonaqueous liquid electrolytes based on quaternary ammonium salts and lithium-ion compounds.[39] Figure 3b compares the Bode plots for the [AMIM][OH]/SU-8 solid electrolyte and the 1M KOH. The characteristic time constants for the two samples were about 8.0 s for the liquid electrolyte and 12.6 s for the patterned ionogel electrolyte, signifying that shorter charge/discharge times may lead to a kinetically limited electrochemical response. Nonetheless, the fact that it is possible to fabricate high spatial resolution patterns of this solid electrolyte with only a small difference in transient response time compared to standard 1M KOH, is very impressive.

A series of experiments was carried out in which the photopatternable [AMIM][TFSI]/SU-8 served as the electrolyte for sputtered VN films, thus enabling the electrochemical properties to be determined. The asprepared VN films exhibit strong preferential crystalline orientation in the (111) direction (Figure S6a) and faceted growth (Figure S6b,c). The intercolumnar porosity from this faceted morphology enables electrolytes in their liquid phase to penetrate throughout the structure (Figure S6d,e, S7). After the [AMIM][TFSI]/SU-8 ionogel electrolyte was patterned directly on top of the planar VN and polymerized, the uniform penetration of the electrolyte was verified by an EDS elemental mapping image (Figure S7), showing that fluorine and sulfur signals originating from the ionic liquids are present throughout the VN layer. The cross-sectional SEM image in Figure S6c indicates that the as-prepared VN electrode thickness was about 5 μm. The surface composition of the VN film, probed by the X-ray photoelectron spectroscopy (XPS) analysis (Figure S6f), is consistent with other VN systems reported in the literature.[32,33]

The charge storage properties of sputtered VN films using the photopatternable solid electrolyte were evaluated in both planar and interdigitated configurations. Linear sweep voltammetry experiments displayed no evidence of electrolyte decomposition between -1.2 and 0.2 V (vs. Hg/HgO) for the photopatternable [AMIM][OH]/SU-8 electrolyte (Figure S4c). The cyclic voltammogram (CV) responses of solid electrolyte patterned VN exhibits the ideal quasi-rectangular capacitive response between 5-20 mV s^{-1} sweep rates over 0.6 V window (Figure 3c). As discussed in previous studies, this pseudocapacitive charge storage behavior arises from redox properties associated with the reduction and oxidation of vanadium between V^{3+} and V^{4+} occurring at the surface or near surface of the VN.[33] Because the electrolyte penetrates the intercolumnar pore network of VN prior to polymerization, the resulting solid electrolyte is in contact with the redox active VN material throughout the entire film and not just at the surface of the film. At a sweep rate of 5 mV s^{-1}, the VN coated with the solid-state electrolyte achieves an areal capacitance of about 0.43 F cm^{-2} which corresponds to 860 F cm^{-3} based on the electrode volume. This areal capacitance is comparable to those reported for CDC films and $Ti_3C_2T_x$ electrodes tested in liquid electrolyte (1M H_2SO_4).[7,40] That is, the solid-state VN electrode exhibited an areal capacitance that exceeds or is on par with high performance supercapacitor materials tested in liquid electrolytes. Moreover, up to a sweep rate of 50 mV s^{-1}, the areal capacitance for VN electrodes with either KOH or solid-state electrolytes are comparable (Figure 3d). Above this sweep rate, the capacitive signature starts to deviate from the ideal shape for both the liquid and solid electrolytes (Figure 3c and S8b). This response can be associated with the fact that the sweep rate of 50 mV s^{-1} corresponds to a 12s charge / discharge cycle time, which matches the characteristic time constant obtained from the Bode plot for the solid electrolyte. The VN electrode paired with the [AMIM][OH]/SU-8 patternable electrolyte also demonstrates excellent long-term cyclability, retaining about 80% of the initial capacitance at 10 mA cm^{-2} by the 10,000th cycle (Figure 3e).

VN interdigitated microdevices were fabricated at the wafer-level as described in the SI (Figure S9a). Figure S9b and Table S3 illustrate the important device parameters for interdigitated cells and fabrication approaches to achieve solid-state microdevices. CV profiles (Figure 4c) of a solid-state interdigitated MSC showed well-defined capacitive behavior over a wide range of scan rates (20 to 200 mV s^{-1}). The areal capacitance of the cell was calculated to be almost 250 mF cm^{-2} at a scan rate of 20 mV s^{-1} and an individual solid-state MSC device was capable of delivering about 10 μWh cm^{-2} in the range of 1-10 mW cm^{-2}. This level of areal capacitance for the solid-state VN MSC is comparable to other interdigitated MSCs tested in liquid electrolytes, including both carbon-based[7] and pseudocapacitive systems (Table S4).[9,41–43] The capacitive behavior of this solid-state microdevice was further studied through galvanostatic measurements at current densities from 2 to 50 mA cm^{-2} (Figure 4d). The galvanostatic profiles at all current densities demonstrated linear behavior, which is a defining feature of a pseudocapacitive material.[44] Figure 4h shows a Ragone plot comparing the performance of solid-state VN MSC to other solid-state MSC devices paired with solid electrolytes such as PVA based hydrogels and silica ionogels.[19,45–48] The results show that VN MSC with the [AMIM][OH]/SU-8 electrolyte achieves better performance in terms of areal energy and power densities compared to previously reported solid-state MSC systems. Moreover, it is important to emphasize that all components of the solid-state VN MSC are defined spatially via lithography, thus enabling miniaturized arrays to be formed in a tiny form factor.

To demonstrate the advantages of semiconductor-based processing, we tested ‘tandem’ MSC microdevices. These interdigitated structures are connected in series and/or parallel configurations using VN layers (without any external wires or deposition of metals) to increase the working cell voltage and/or total current response of an integrated microdevice (Figure 4 e-g). The ability to integrate multiple MSCs in a small footprint area is achieved because spatial control of the photopatternable hydroxide-conducting solid electrolyte effectively prevents leakage current between individual MSC devices. The tandem microdevice in a series configuration demonstrated reliable cycling over a 1.2 V window, twice the voltage of a single MSC device. Accordingly, the total capacitance for the tandem device increased to over 11 mF. As expected, a parallel configuration provided twice the current response compared to a single MSC device. Capacitive behavior was maintained throughout a 0.6 V window in both cyclic voltammetry and galvanostatic experiments, producing a total current above 1 mA. Unfortunately, the circuit layout for the microfabricated wafer did not allow us to evaluate more than four devices in either parallel or series configuration. Nonetheless, these electrochemical measurements made on tandem VN-MSC microdevices confirm that the cell voltage range and total current output of MSC devices can be tailored easily by modifying the device configurations. Considering that all components in this solid-state tandem energy storage system are fully processed with semiconductor-based fabrication techniques, the approach shown here provides the basis for achieving miniaturized energy-storage systems that can be incorporated with densely packed integrated circuits without compromising their electrochemical properties.

It is interesting to consider the prospect of using miniaturized EES systems to power IoT devices. In particular, to power a sensor node platform (MICA2 and IMote2), as an example, an average power consumption for these sensor nodes are 3 and 12 mW with the peak power requirement of 60 and 250 mW, respectively.[49] It becomes clear that a single 4 mm^2 solid VN MSC device that is capable of delivering 110 mW cm^{-2} is still far below the power requirements for commercial sensor nodes, especially with regard to the limited energy density it provides (~ 10 μWh cm^{-2}). However, the demonstrated tandem approach to MSCs suggests a viable solution as the footprint area of these sensor nodes is around 18 cm^2. Thus, fabricating MSCs at wafer-scale offers the prospect of providing the energy and power requirements for this basic IoT component. To be sure, there are still a number of challenges that need to be addressed in order to realize this micropower system, but the basic elements of using a single VN material to be both redox-active electrodes and interconnects, coupled with the photopatternable, hydroxide ion conducting solid electrolyte provide the basis for enhancing micropower technology.

Conclusion

Among the few hydroxide ion conducting solid electrolytes reported to date, none offer the combination of high room temperature ionic conductivity (10 mS cm^{-1}), excellent thermal stability, mechanical integrity, and the photopatterning capability of the [AMIM][OH]/SU-8 solid electrolyte presented here. The ion transport properties of this electrolyte and ability to carry out charge transfer at the electrolyte/electrode interface were validated using hydroxide-based redox-active $NiCo_2O_4$ and VN. For device-level demonstration, [AMIM][OH]/SU-8 hydroxide-conducting solid electrolyte was directly patterned onto VN MSC electrodes to create both individual and tandem devices. The performance of individual MSC devices of nearly 250 mF cm^{-2} at 20 mV s^{-1} sweep rate goes beyond what has been reported for interdigitated MSC devices with liquid electrolytes and underscores the significance of this solid electrolyte. Electrochemical testing of tandem micro-supercapacitor devices has shown that the potential range and total current output of micro-supercapacitor devices can be tailored by modifying the device arrangements in appropriate series or parallel configurations. Finally, the semiconductor processing methods demonstrated here hold promise for achieving the power and energy density demands for IoT technology.

Experimental Procedures

Resource availability

Lead contact: Further information and requests for resources and materials should be directed to and will be fulfilled by the lead contact, Bruce Dunn (bdunn@ucla.edu).

Materials availability: This study did not generate new unique materials.

Data and Code Availability: Much of the data presented in this work is available by request from the lead contact. This study did not generate any code for analysis.

Materials: 1-Allyl-3H-imidazolium bis(trifluoromethanesulfonyl)imide ([AMIM][TFSI], 99% purchased from Solvionic), SU-8 3000 (purchased from MicroChem), KOH (purchased from Alfa-Aesar), and dimethyl sulfoxide (DMSO, 99.9% purchased from Sigma Aldrich) were used as received.

Photopatternable Hydroxide-Conducting Solid Electrolyte Preparation: All sample preparation was carried out in class 100 clean room with yellow lighting to reduce the exposure of the materials to shorter wavelengths. [AMIM][TFSI] SU 8 was prepared by mixing 40 weight percent [AMIM][TFSI] and SU 8 prior to deposition. Films prepared for electrochemical measurements were spin coated onto flat substrates (i.e. Si/SiO$_2$ or VN) at 500 rpm for 5 s followed by 3000 rpm for 30 s. Samples were then soft baked at 95 °C for 5 min for solvent removal prior to patterning. Features were patterned using a Karl Suss MA6 Contact Aligner and photomask. The [AMIM][TFSI] SU 8 samples were subjected to a total of 1600 mW of UV exposure at 365 nm. The films were then postexposure baked at 95 °C for 5 min to crosslink the material (40% [AMIM][TFSI/SU-8). UV exposed samples were then developed. For the anion exchange process, photopatterned [AMIM][TFSI]/SU-8 electrolytes were soaked in DMSO to swell the crosslinked polymer for a minimum of 1 hr. Subsequent soaking in 1M KOH replaced TFSI$^-$ in the structure with OH$^-$ (40% [AMIM][OH]/SU-8).

Physical and Chemical Characterizations: FTIR spectroscopy was carried out using a Jasco 6100 with a 4 cm^{-1} spectral resolution from 4000 to 500 cm^{-1}. The photopatternable electrolyte was prepared on IR transparent polytetrafluoroethylene films for the measurement. Nanoindentation measurements were made using an MTS Nano Indenter XP Instrument with a Berkovich indenter to determine the elastic modulus of hydroxide-conducting SU 8 films. Samples were indented to a depth of 2 µm at 20 different locations. The elastic modulus was determined using a Poisson's ratio of 0.22 for SU 8 and the Oliver and Pharr analysis. Film thicknesses were measured using a Dektak 6 surface profilometer. TGA was performed using an Instrument Specialists thermogravimetric analyzer tool in air at a heating rate of 10 ◦C min^{-1}. Scanning electron microscope (SEM) was performed using an FEI Nova 230 Nano with attached EDS. XPS analysis was carried out using a Kratos Axis Ultra DLD with a monochromatic Al Kα radiation source. The charge neutralizer filament was used to control charging of the sample, a 20 eV pass energy was used with a 0.05 eV step size, and all scans were calibrated using the C 1s peak shifted to 284.8 eV. The integrated area of the peaks was found using the CasaXPS software.

Synthesis of NiCo$_2$O$_4$: NiCo$_2$O$_4$ was prepared using a one-step microwave synthesis. Nickel nitrate hexahydrate (0.15 g, Sigma-Aldrich) and cobalt nitrate hexahydrate (0.18 g, Sigma-Aldrich) precursors were dissolved in deionized water (5 ml), and ethylene glycol (17.5 ml) and urea (0.1 g, Sigma-Aldrich) were added in this solution with stirring. The homogeneous solution was then transferred into the 30 ml microwave reaction vessel and placed in a microwave synthesis system (Discover SP, CEM Corporation). The sample was heated to 140 °C for 30 min. The resulting green-colored solution was centrifuged and washed with deionized water and ethanol and dried in vacuum for 24 h. The samples were then fully oxidized by annealing the as-prepared samples at 300 °C for 1 h.

Vanadium Nitride Electrode Preparation: To prevent electrical short-circuits and chemical etching from basic electrolytes, a 500 nm-thick Si_3N_4 layer was deposited by low pressure chemical vapor deposition at 800 °C to protect the Si wafer. The VN thin films were then deposited by reactive magnetron sputtering using a 4-inch target of pure metallic vanadium in an Alliance Concept CT-200 reactor. Prior to deposition, the pressure of the chamber was kept below 10^{-6} mbar and the target-substrate was fixed at 6 cm. The deposition parameters were fixed at 100°C for the temperature, 25 and 5 sccm for the argon and nitrogen flow rates, 7.5 x 10^{-3} mbar for the deposition pressure, and 2 W.cm^{-2} for the power density. The deposition time was tuned to achieve 5µm-thick VN thick films. The typical loading of the VN electrode film was 2.5 mg cm^{-2}.

Fabrication of the symmetric interdigitated micro-supercapacitor (MSC): After the deposition of the Si_3N_4 (500 nm) and the VN (5 µm) thin films, photoresist was spin-coated to form the resist mask. The VN was etched using Inductively Coupled Plasma Reactive Ion Etching (ICP RIE) process using a mixture of chlorine/argon gases (Cl_2 / Ar). To avoid short-circuits between the interdigitated VN electrodes, the etching was stopped once the top 10 nm of the Si_3N_4 layer was etched. Due to this four-step process, 40 MSCs can be fabricated on a single 3-inch silicon wafer (7.5 cm diameter / thickness = 0.385 mm).

Electrochemical Characterization: All electrochemical measurements were using a Bio Logic VMP 3 Potentiostat. Electrochemical impedance spectroscopy (EIS) was performed on a VN/[AMIM][OH]SU8/VN 2-electrode cell between 1 MHz and 5 mHz using a 10 mV amplitude and 0 V bias. Linear-sweep voltammetry (LSV) was used to evaluate the electrochemical stability window of the [AMIM][OH]/SU-8

using a solid electrolyte coated glassy carbon as a working electrode. LSV was conducted from the open circuit voltage (OCV) to 0.7 V (vs. Hg/HgO) and from OCV to −1.4 V at a sweep rate of 10 mV s^{-1}. For the CV and galvanostatic cycling measurements, the planar VN film (deposited directed on a Si/Si_3N_4 wafer) was tested in 1M KOH using a conventional 3-electrode set-up. A Hg/HgO reference electrode and a Pt foil were used as a reference electrode and counter electrode, respectively. For the solid-state samples, 10 µm thick film of the photopatternable electrolyte was directly patterned onto the VN and tested using the same cell configuration. For the electrochemical testing of interdigitated devices, the 2-electrode measurement was carried out using a standard probe station with the sample stationed on an air table.

Acknowledgements

The research was supported by the Office of Naval Research (N00014-19-1-2113). This project has received financial support from the CNRS through the MITI interdisciplinary programs. The authors also want to thank the ANR STORE-EX and the French network on electrochemical energy storage (RS2E) for the financial support. The French RENATECH network is greatly acknowledged for the use of microfabrication facilities.

Author contributions

Conceptualization, C.C., C.L., and B.D.; Methodology, C.C., K.R., C.L., and B.D.; Investigation, C.C., K.R., G.W., and P.R.; Writing – Original Draft, C.C. and B.D.; Writing – Review & Editing, C.C., K.R., G.W., C.L., and B.D.; Funding Acquisition, C.L. and B.D.; Supervision, C.L. and B.D.

Declaration of interests

The authors declare no competing interests.

References

1. Liu, H., Zhang, G., Zheng, X., Chen, F., and Duan, H. (2020). Emerging miniaturized energy storage devices for microsystem applications: from design to integration. Int. J. Extrem. Manuf. *2*, 042001.

2. Fan, X., Liu, X., Hu, W., Zhong, C., and Lu, J. (2019). Advances in the development of power supplies for the Internet of Everything. InfoMat, inf2.12016.

3. Jayakumar, H., Lee, K., Lee, W.S., Raha, A., Kim, Y., and Raghunathan, V. (2014). Powering the internet of things. In Proceedings of the 2014 international symposium on Low power electronics and design - ISLPED ’14 (ACM Press), pp. 375–380.

4. Rolison, D.R., and Nazar, L.F. (2011). Electrochemical energy storage to power the 21st century. MRS Bull. *36*, 486–493.

5. Hur, J.I., Smith, L.C., and Dunn, B. (2018). High Areal Energy Density 3D Lithium-Ion Microbatteries. Joule *2*, 1187–1201.

6. Choi, C.S., Lau, J., Hur, J., Smith, L., Wang, C., and Dunn, B. (2018). Synthesis and Properties of a Photopatternable Lithium-Ion Conducting Solid Electrolyte. Adv. Mater. *30*, 1703772.

7. Huang, P., Lethien, C., Pinaud, S., Brousse, K., Laloo, R., Turq, V., Respaud, M., Demortiere, A., Daffos, B., Taberna, P.L., et al. (2016). On-chip and freestanding elastic carbon films for microsupercapacitors. Science *351*, 691–695.

8. Beidaghi, M., and Wang, C. (2012). Micro-Supercapacitors Based on Interdigital Electrodes of Reduced Graphene Oxide and Carbon Nanotube Composites with Ultrahigh Power Handling Performance. Adv. Funct. Mater. *22*, 4501–4510.

9. Robert, K., Douard, C., Demortière, A., Blanchard, F., Roussel, P., Brousse, T., and Lethien, C. (2018). On Chip Interdigitated Micro-Supercapacitors Based on Sputtered Bifunctional Vanadium Nitride Thin Films with Finely Tuned Inter- and Intracolumnar Porosities. Adv. Mater. Technol. *3*, 1800036.

10. Eustache, E., Douard, C., Demortière, A., De Andrade, V., Brachet, M., Le Bideau, J., Brousse, T., and Lethien, C. (2017). High Areal Energy 3D-Interdigitated Micro-Supercapacitors in Aqueous and Ionic Liquid Electrolytes. Adv. Mater. Technol. *2*, 1700126.

11. Ning, H., Pikul, J.H., Zhang, R., Li, X., Xu, S., Wang, J., Rogers, J.A., King, W.P., and Braun, P.V. (2015). Holographic patterning of high-performance on-chip 3D lithium-ion microbatteries. Proc Natl Acad Sci USA *112*, 6573–6578.

12. Ashby, D.S., Choi, C.S., Edwards, M.A., Talin, A.A., White, H.S., and Dunn, B.S. (2020). HighPerformance Solid-State Lithium-Ion Battery with Mixed 2D and 3D Electrodes. ACS Appl. Energy Mater., acsaem.0c01029.

13. Létiche, M., Eustache, E., Freixas, J., Demortière, A., De Andrade, V., Morgenroth, L., Tilmant, P., Vaurette, F., Troadec, D., Roussel, P., et al. (2017). Atomic Layer Deposition of Functional Layers for on Chip 3D Li-Ion All Solid State Microbattery. Adv. Energy Mater. *7*, 1601402.

14. Zhong, C., Deng, Y., Hu, W., Qiao, J., Zhang, L., and Zhang, J. (2015). A review of electrolyte materials and compositions for electrochemical supercapacitors. Chem. Soc. Rev. *44*, 7484–7539.

15. Li, J., Qiao, J., and Lian, K. (2020). Hydroxide ion conducting polymer electrolytes and their applications in solid supercapacitors: A review. Energy Storage Materials *24*, 6–21.

16. Dubal, D.P., Chodankar, N.R., Kim, D.-H., and Gomez-Romero, P. (2018). Towards flexible solidstate supercapacitors for smart and wearable electronics. Chem. Soc. Rev. *47*, 2065–2129.

17. Alipoori, S., Mazinani, S., Aboutalebi, S.H., and Sharif, F. (2020). Review of PVA-based gel polymer electrolytes in flexible solid-state supercapacitors: Opportunities and challenges. Journal of Energy Storage *27*, 101072.

18. Le Bideau, J., Viau, L., and Vioux, A. (2011). Ionogels, ionic liquid based hybrid materials. Chem. Soc. Rev. *40*, 907–925.

19. Asbani, B., Bounor, B., Robert, K., Douard, C., Athouël, L., Lethien, C., Le Bideau, J., and Brousse, T. (2020). Reflow Soldering-Resistant Solid-State 3D Micro-Supercapacitors Based on Ionogel Electrolyte for Powering the Internet of Things. J. Electrochem. Soc. *167*, 100551.

20. Beidaghi, M., and Gogotsi, Y. (2014). Capacitive energy storage in micro-scale devices: recent advances in design and fabrication of micro-supercapacitors. Energy Environ. Sci. *7*, 867.

21. Ashby, D.S., DeBlock, R.H., Lai, C.-H., Choi, C.S., and Dunn, B.S. (2017). Patternable, SolutionProcessed Ionogels for Thin-Film Lithium-Ion Electrolytes. Joule *1*, 344–358.

22. Nishimura, N., and Ohno, H. (2014). 15th anniversary of polymerised ionic liquids. Polymer *55*, 3289–3297.

23. Umeshbabu, E., Rajeshkhanna, G., and Rao, G.R. (2014). Urchin and sheaf-like NiCo 2 O 4 nanostructures: Synthesis and electrochemical energy storage application. International Journal of Hydrogen Energy *39*, 15627–15638.

24. Ding, R., Qi, L., and Wang, H. (2012). A facile and cost-effective synthesis of mesoporous NiCo2O4 nanoparticles and their capacitive behavior in electrochemical capacitors. J Solid State Electrochem *16*, 3621–3633.

25. Wu, G.M., Lin, S.J., and Yang, C.C. (2006). Preparation and characterization of PVA/PAA membranes for solid polymer electrolytes. Journal of Membrane Science *275*, 127–133.

26. Tran, T.N.T., Clark, M.P., Chung, H., and Ivey, D.G. (2020). Effects of Crosslinker Concentration in Poly(Acrylic Acid) KOH Gel Electrolyte on Performance of Zinc Air Batteries. Batteries & Supercaps *3*, 409–416.

27. Cao, Z., Hu, H., Wu, M., Tang, K., and Jiang, T. (2019). Planar all-solid-state rechargeable Zn–air batteries for compact wearable energy storage. J. Mater. Chem. A *7*, 17581–17593.

28. Zhang, S.S. (2007). A review on the separators of liquid electrolyte Li-ion batteries. Journal of Power Sources *164*, 351–364.

29. Kalnaus, S., Wang, Y., and Turner, J.A. (2017). Mechanical behavior and failure mechanisms of Liion battery separators. Journal of Power Sources *348*, 255–263.

30. Huo, P., Zhang, S., Zhang, X., Geng, Z., Luan, J., and Wang, G. (2015). Quaternary ammonium functionalized poly(aryl ether sulfone)s as separators for supercapacitors based on activated carbon electrodes. Journal of Membrane Science *475*, 562–570.

31. Zeng, L., Zhao, T.S., An, L., Zhao, G., and Yan, X.H. (2015). Physicochemical properties of alkaline doped polybenzimidazole membranes for anion exchange membrane fuel cells. Journal of Membrane Science *493*, 340–348.

32. Choi, D., Blomgren, G.E., and Kumta, P.N. (2006). Fast and Reversible Surface Redox Reaction in Nanocrystalline Vanadium Nitride Supercapacitors. Adv. Mater. *18*, 1178–1182.

33. Robert, K., Stiévenard, D., Deresmes, D., Douard, C., Iadecola, A., Troadec, D., Simon, P., Nuns, N., Marinova, M., Huvé, M., et al. (2020). Novel insights into the charge storage mechanism in pseudocapacitive vanadium nitride thick films for high-performance on-chip micro-supercapacitors. Energy Environ. Sci. *13*, 949–957.

34. Yang, C.-C., Hsu, S.-T., and Chien, W.-C. (2005). All solid-state electric double-layer capacitors based on alkaline polyvinyl alcohol polymer electrolytes. Journal of Power Sources *152*, 303–310.

35. Lewandowski, A. (2001). Supercapacitor based on activated carbon and polyethylene oxide–KOH–H2O polymer electrolyte. Electrochimica Acta *46*, 2777–2780.

36. Gao, H., Li, J., and Lian, K. (2014). Alkaline quaternary ammonium hydroxides and their polymer electrolytes for electrochemical capacitors. RSC Adv. *4*, 21332–21339.

37. Li, J., Qiao, J., and Lian, K. (2017). Investigation of polyacrylamide based hydroxide ion-conducting electrolyte and its application in all-solid electrochemical capacitors. Sustainable Energy Fuels *1*, 1580–1587.

38. Yang, H.M., Kwon, Y.K., Lee, S.B., Kim, S., Hong, K., and Lee, K.H. (2017). Physically CrossLinked Homopolymer Ion Gels for High Performance Electrolyte-Gated Transistors. ACS Appl. Mater. Interfaces *9*, 8813–8818.

39. Ue, M., Ida, K., and Mori, S. (1994). Electrochemical Properties of Organic Liquid Electrolytes Based on Quaternary Onium Salts for Electrical Double Layer Capacitors. J. Electrochem. Soc. *141*, 2989–2996.

40. Ghidiu, M., Lukatskaya, M.R., Zhao, M.-Q., Gogotsi, Y., and Barsoum, M.W. (2014). Conductive two-dimensional titanium carbide 'clay' with high volumetric capacitance. Nature *516*, 78–81.

41. El-Kady, M.F., Ihns, M., Li, M., Hwang, J.Y., Mousavi, M.F., Chaney, L., Lech, A.T., and Kaner, R.B. (2015). Engineering three-dimensional hybrid supercapacitors and microsupercapacitors for high-performance integrated energy storage. Proc Natl Acad Sci USA *112*, 4233–4238.

42. Tian, W., VahidMohammadi, A., Reid, M.S., Wang, Z., Ouyang, L., Erlandsson, J., Pettersson, T., Wågberg, L., Beidaghi, M., and Hamedi, M.M. (2019). Multifunctional Nanocomposites with High Strength and Capacitance Using 2D MXene and 1D Nanocellulose. Adv. Mater. *31*, 1902977.

43. Li, J., Shi, Q., Shao, Y., Hou, C., Li, Y., Zhang, Q., and Wang, H. (2019). Cladding nanostructured AgNWs-MoS2 electrode material for high-rate and long-life transparent in-plane microsupercapacitor. Energy Storage Materials *16*, 212–219.

44. Choi, C., Ashby, D.S., Butts, D.M., DeBlock, R.H., Wei, Q., Lau, J., and Dunn, B. (2020). Achieving high energy density and high power density with pseudocapacitive materials. Nat Rev Mater *5*, 5–19.

45. El-Kady, M.F., and Kaner, R.B. (2013). Scalable fabrication of high-power graphene microsupercapacitors for flexible and on-chip energy storage. Nat Commun *4*, 1475.

46. Wang, S., Hsia, B., Carraro, C., and Maboudian, R. (2014). High-performance all solid-state microsupercapacitor based on patterned photoresist-derived porous carbon electrodes and an ionogel electrolyte. J. Mater. Chem. A *2*, 7997–8002.

47. Wang, Y., Sun, L., Xiao, D., Du, H., Yang, Z., Wang, X., Tu, L., Zhao, C., Hu, F., and Lu, B. (2020). Silicon-Based 3D All-Solid-State Micro-Supercapacitor with Superior Performance. ACS Appl. Mater. Interfaces *12*, 43864–43875.

48. Brousse, K., Pinaud, S., Nguyen, S., Fazzini, P., Makarem, R., Josse, C., Thimont, Y., Chaudret, B., Taberna, P., Respaud, M., et al. (2020). Facile and Scalable Preparation of Ruthenium Oxide Based Flexible Micro Supercapacitors. Adv. Energy Mater. *10*, 1903136.

49. Hancke, G., Silva, B., and Hancke, Jr., G. (2012). The Role of Advanced Sensing in Smart Cities. Sensors *13*, 393–425.

Figure 1

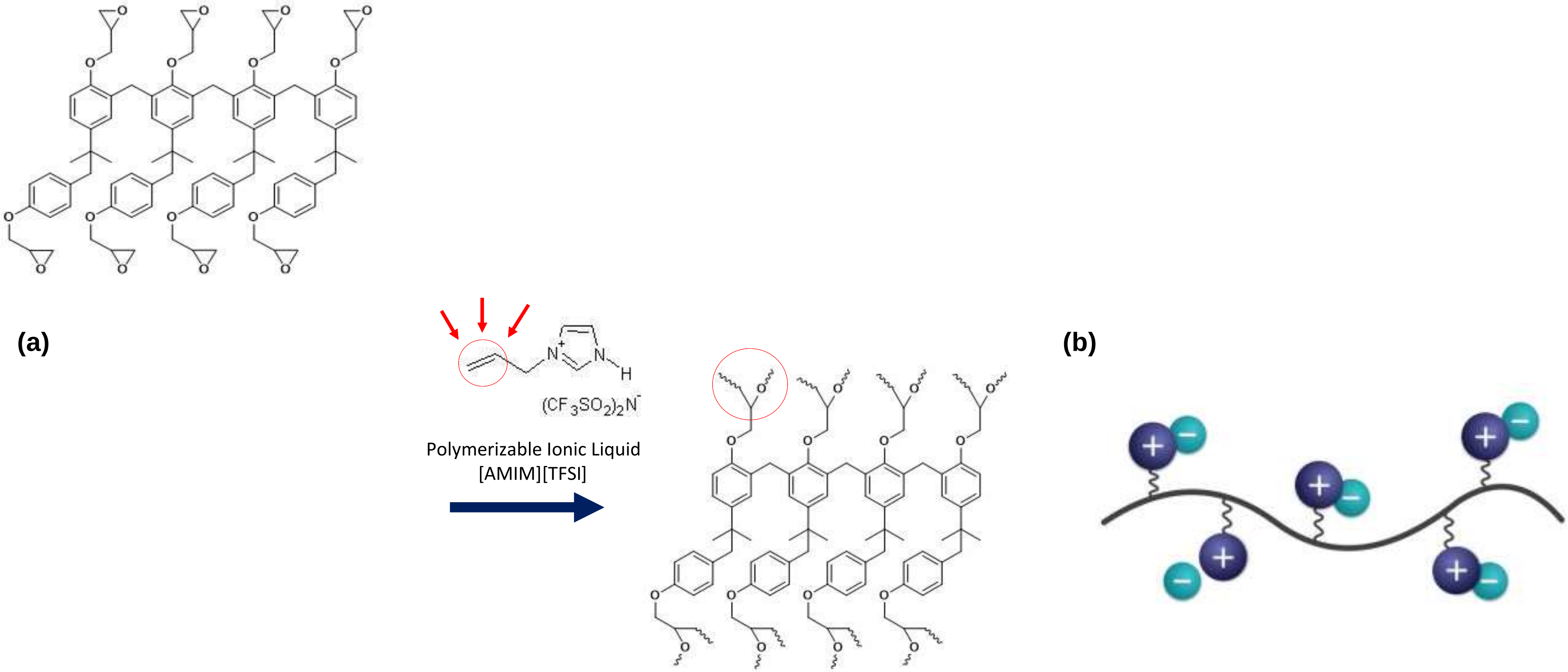

Figure 2

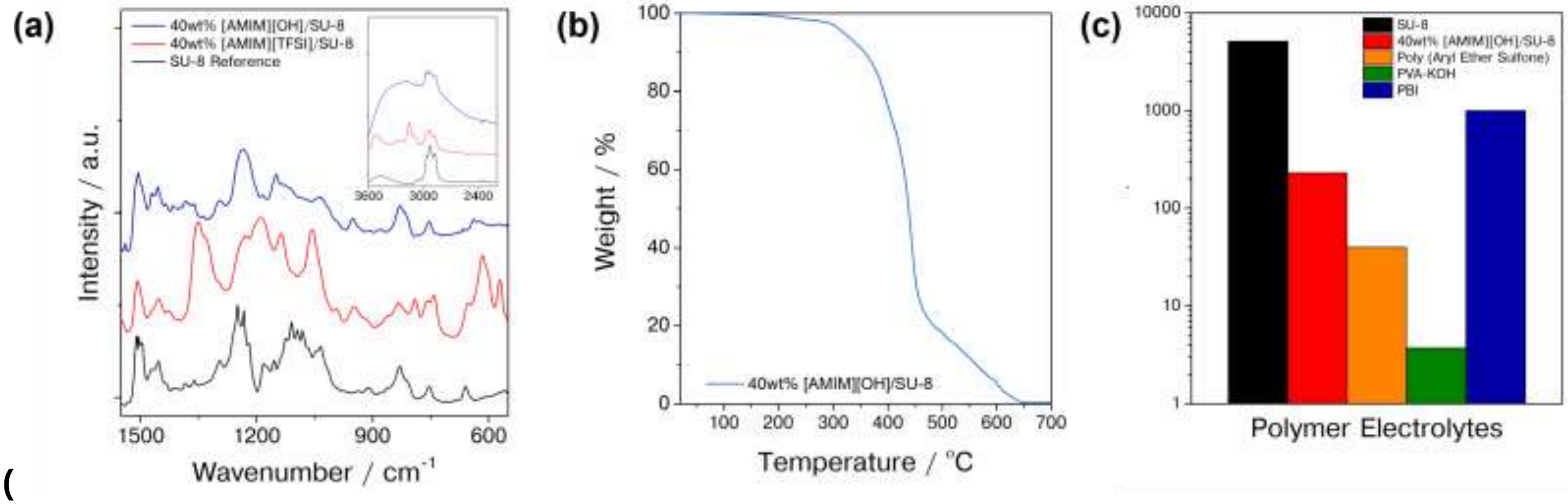
(a)
40wt% [AMIM][OH]/SU-8
40wt% [AMIM][TFSI]/SU-8
SU-8 Reference
3600
3000
2400
Intensity / a.u.
1500
1200
900
600
Wavenumber / cm^{-1}
(b)
100
80
60
40
20
0
Weight / %
40wt% [AMIM][OH]/SU-8
100
200
300
400
500
600
700
Temperature / °C
(c)
10000
1000
100
10
1
SU-8
40wt% [AMIM][OH]/SU-8
Poly (Aryl Ether Sulfone)
PVA-KOH
PBI
Polymer Electrolytes

(a)

Figure 3

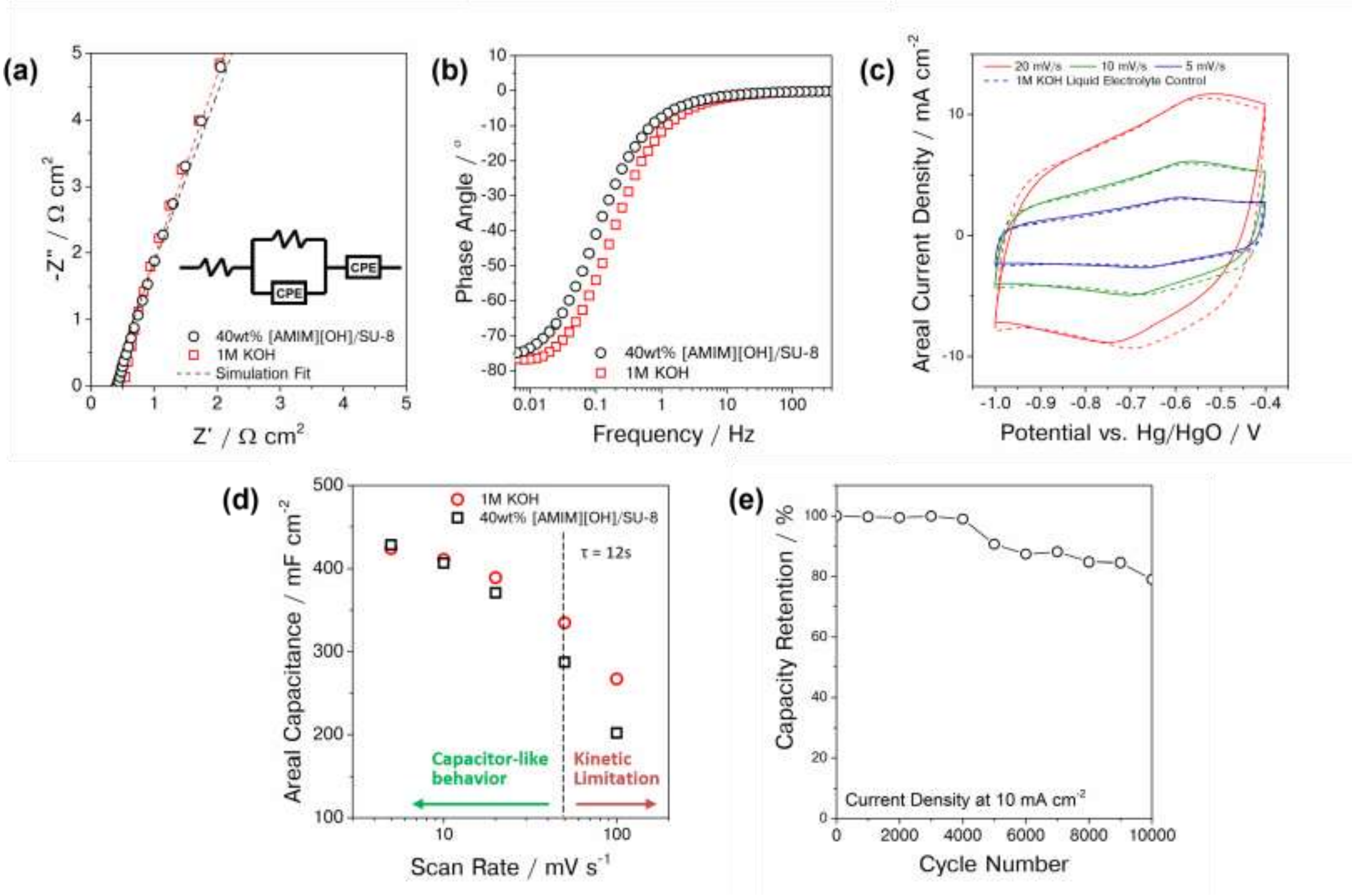
(a)
-Z" / Ω cm2
Z' / Ω cm2
CPE
CPE
40wt% [AMIM][OH]/SU-8
1M KOH
Simulation Fit
0
1
2
3
4
5
(b)
Phase Angle / °
Frequency / Hz
40wt% [AMIM][OH]/SU-8
1M KOH
10
0
-10
-20
-30
-40
-50
-60
-70
-80
0.01
0.1
1
10
100
(c)
Areal Current Density / mA cm-2
Potential vs. Hg/HgO / V
20 mV/s
10 mV/s
5 mV/s
1M KOH Liquid Electrolyte Control
10
0
-10
-1.0
-0.9
-0.8
-0.7
-0.6
-0.5
-0.4
(d)
Areal Capacitance / mF cm-2
Scan Rate / mV s-1
1M KOH
40wt% [AMIM][OH]/SU-8
τ = 12s
Capacitor-like behavior
Kinetic Limitation
500
400
300
200
100
10
100
(e)
Capacity Retention / %
Cycle Number
Current Density at 10 mA cm-2
100
80
60
40
20
0
0
2000
4000
6000
8000
10000

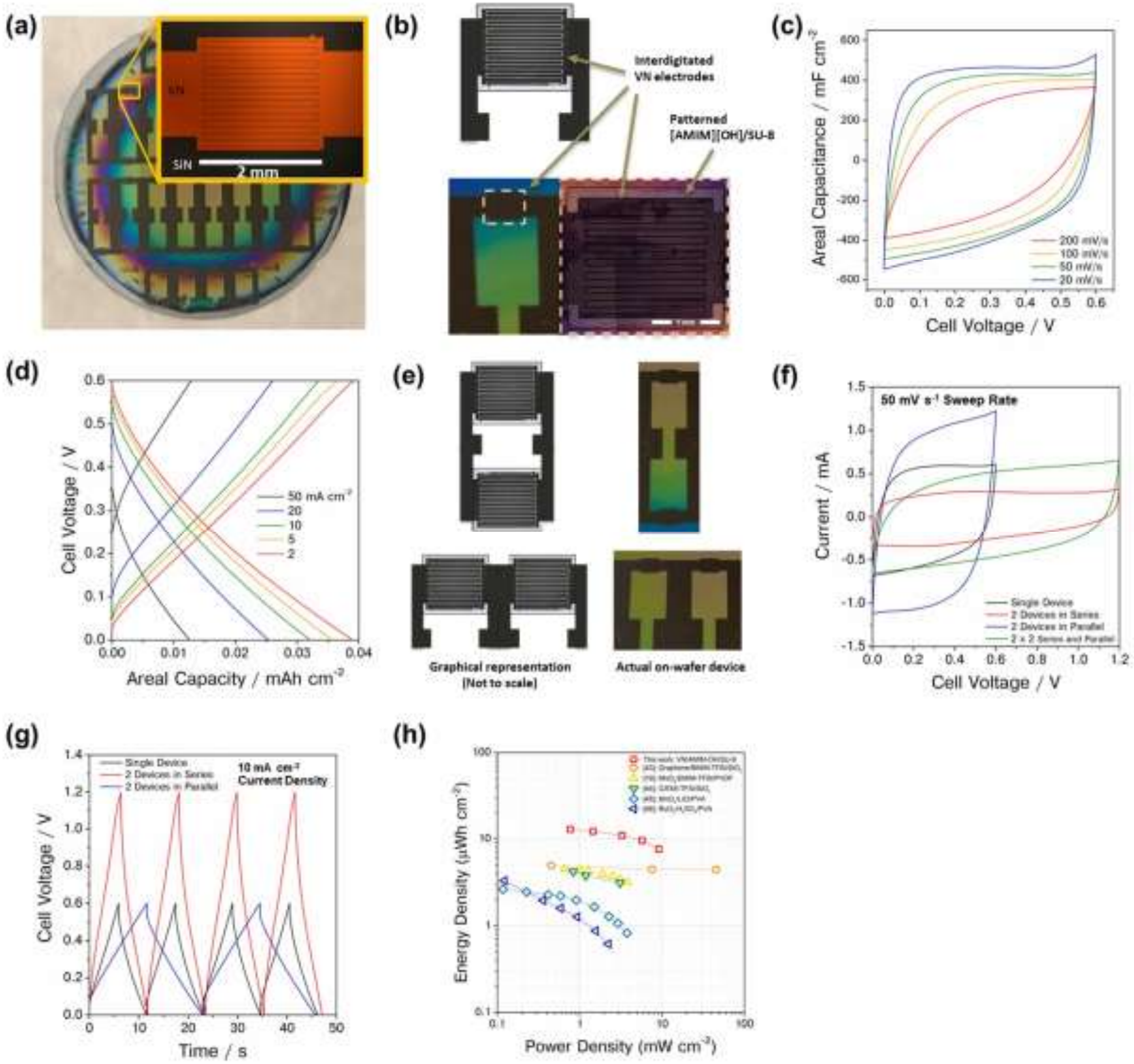
(a)
SiN
SiN
2 mm
(b)
Interdigitated VN electrodes
Patterned [AMIM][OH]/SU-8
(c)
Areal Capacitance / mF cm^{-2}
Cell Voltage / V
200 mV/s
100 mV/s
50 mV/s
20 mV/s
(d)
Cell Voltage / V
Areal Capacity / mAh cm^{-2}
50 mA cm^{-2}
20
10
5
2
(e)
Graphical representation (Not to scale)
Actual on-wafer device
(f)
50 mV s^{-1} Sweep Rate
Current / mA
Cell Voltage / V
Single Device
2 Devices in Series
2 Devices in Parallel
2 x 2 Series and Parallel
(g)
Cell Voltage / V
Time / s
Single Device
2 Devices in Series
2 Devices in Parallel
10 mA cm^{-2} Current Density
(h)
Energy Density (µWh cm^{-2})
Power Density (mW cm^{-2})

Figure 4

Figure Captions:

Figure 1. (a) The chemical structure of SU-8 photoresist before and after the UV-induced polymerization. The polymerizable ionic liquid [AMIM][TFSI] is in-situ grafted during this process. (b) Schematic diagram of polymerized ionic liquids with charge-carrying mobile anions.[22]

Figure 2. (a) FT-IR of the photopatterned electrolytes before (red) and after (blue) the hydroxide anion exchange. Once the anions exchanged, the infrared absorbance bands of TFSI anions disappeared as those of OH^- emerged. It is should be noted that the characteristic peaks of polymerized cations are still present after this process (Table S2). (b) TGA of ionic liquid modified SU-8. The [AMIM][OH]/SU-8 patternable electrolyte exhibits excellent thermal stability up to 320 °C in air. (c) Mechanical properties of [AMIM][OH]/SU-8 films measured by nanoindentation compared with other hydroxide conducting solid electrolytes.[25,30,31] The elastic modulus of [AMIM][OH]/SU-8 was 230 MPa.

Figure 3. (a) Impedance spectra of [AMIM][OH]/SU-8 and 1M KOH. The ionic conductivity value determined for the patterned electrolyte was 10 mS cm^{-1}. (b) Bode plot for the two electrolyte systems. The characteristic time constants determined from the transition frequency for two samples were about 8 s for the liquid electrolyte control and 12.6 s for the patterned electrolyte. (c) CV profile of the [AMIM][OH]/SU-8 solid electrolyte patterned VN electrode at sweep rates of 5 to 20 mV s^{-1}. The dashed lines of the same color represent the CV results from the 1M KOH liquid electrolyte which serves as a control. (d) Comparison of the areal capacitance vs. sweep rate for planar VN electrodes using 1M KOH and [AMIM][OH]/SU-8 patternable electrolytes. At scan rates below 50 mV s^{-1}, the areal capacitance values are nearly identical. (e) Long-term galvanostatic cycling of the solid electrolyte patterned VN electrode at a 10 mA cm^{-2} current density.

Figure 4. (a) A photograph of wafer-scale fabricated interdigitated VN MSC devices. 40 individual interdigitated devices are fabricated per a 3” Si wafer. The solid-state device configurations for (b) a single MSC device and (e) two MSC units connected in parallel and in series. (c) Cyclic voltammetry of a symmetric solid-state MSC device at sweep rates of 20 to 200 mV s^{-1} over 0.6 V window. (d) Galvanostatic charge–discharge curves of a symmetric solid-state MSC device at various areal current densities. The solid-state MSC device exhibits a linear behavior at all current densities. (f) CV curves of MSC devices configured in various series and parallel arrangement. Various configurations show a capacitor-like rectangular feature, indicating an ideal capacitive behavior. (g) Galvanostatic profiles of tandem MSC devices connected in various series or parallel arrangement compared with a single MSC device. (h) Areal energy and

power densities of solid-state VN MSC compared with other highperformance solid-state MSC systems. Our solid VN MSC demonstrates the highest areal energy and power densities, delivering about 10 µWh cm^{-2} in the range of 1-10 mW cm^{-2}. The legend lists the active materials/ionic species/solid host material.

Figure Legends:

Figure 2. (a) 40wt% [AMIM][OH]/SU-8; 40wt% [AMIM][TFSI]/SU-8; SU-8 Reference (b) 40wt% [AMIM][OH]/SU-8 (c) SU-8; 40wt% [AMIM][OH]/SU-8; Poly (Aryl Ether Sulfone); PVA-KOH; PBI

Figure 3. (a) 40wt% [AMIM][OH]/SU-8; 1M KOH (b) 40wt% [AMIM][OH]/SU-8; 1M KOH (c) 20 mV/s; 10 mV/s; 5 mV/s; 1M KOH Liquid Electrolyte Control (d) 1M KOH; 40wt% [AMIM][OH]/SU-8

Figure 4. (c) 200 mV/s; 100 mV/s; 50 mV/s; 20 mV/s (d) 50 mA cm^{-2}; 20; 10; 5; 2 (f) Single Device; 2 Devices in Series; 2 Devices in Parallel; 2 x 2 Series and Parallel (g) Single Device; 2 Devices in Series; 2 Devices in Parallel (h) This work: VN/AMIM-OH/SU-8; [43]: Graphene/BMIM-TFSI/SiO_2; [19]: MnO_2/EMIM-TFSI/PVDF; [44]: C/EMI-TFSI/SiO_2; [45]: MnO_2/LiCl/PVA; [46]: RuO_2/H_2SO_4/PVA

Survey of miniaturized electrochemical energy storage systems

Miniaturized electrochemical energy storage (EES) systems, in general, have great design flexibility and have been manufactured by a range of fabrication techniques, leading to various device form factors with multiple functionalities without deterioration in performance.[1–3] Recent advances in the community have included the demonstration of novel fabrication approaches and unique battery designs, and the incorporation of solid electrolytes (Table S1).[4–11]

Table S1. Summary of Notable Miniaturized Electrochemical Energy Storage Systems

Classification	Materials	Electrolytes	Fabrication Approaches	Functionality	Energy Density [uWh/cm^2] (Power Density in [mW/cm^2])	Ref.
Micro-Supercapacitor	RuO_2	PVA/H_2SO_4	Microfabrication	Planar design, on-chip	0.48 (50)	4
Micro-Supercapacitor	MnO_2	0.5M Na_2SO_4	Microfabrication	Planar design, on-chip	10 (20)	5
Micro-Supercapacitor	$Ti_3C_2T_x$	PVA/H_2SO_4	3D Printing	Planar design, on-chip	54.3 (5.7)	6
Micro-Supercapacitor	$Ti_3C_2T_x$	PVA/H_2SO_4	3D Printing	Planar design, on-chip	24.4 (0.64)	7
Stretchable Supercapacitor	Graphene	PVP/NaCl	Laser-Writing	Stretchable	0.09 (0.02)	8
3D Microbattery	$LiFePO_4$/Li metal	1M LiTFSI in DOL/DME	3D Printing	Planar design, on-chip	225.7 (0.02)	9
Coaxial Fiber-Shaped Battery	$LiFePO_4$/$Li_4Ti_5O_{12}$	$LiPF_6$ in EC/DMC in PVDF-co-HFP	3D Printing	Flexible, unique design	2596.6 (0.22)	10
Coaxial Fiber-Shaped Supercapacitor	V_2O_5/VN	PVA/KOH	3D Printing	Flexible, unique design	54.3 (0.80)	11

Synthesis and properties of hydroxide conducting photopatternable solid electrolytes

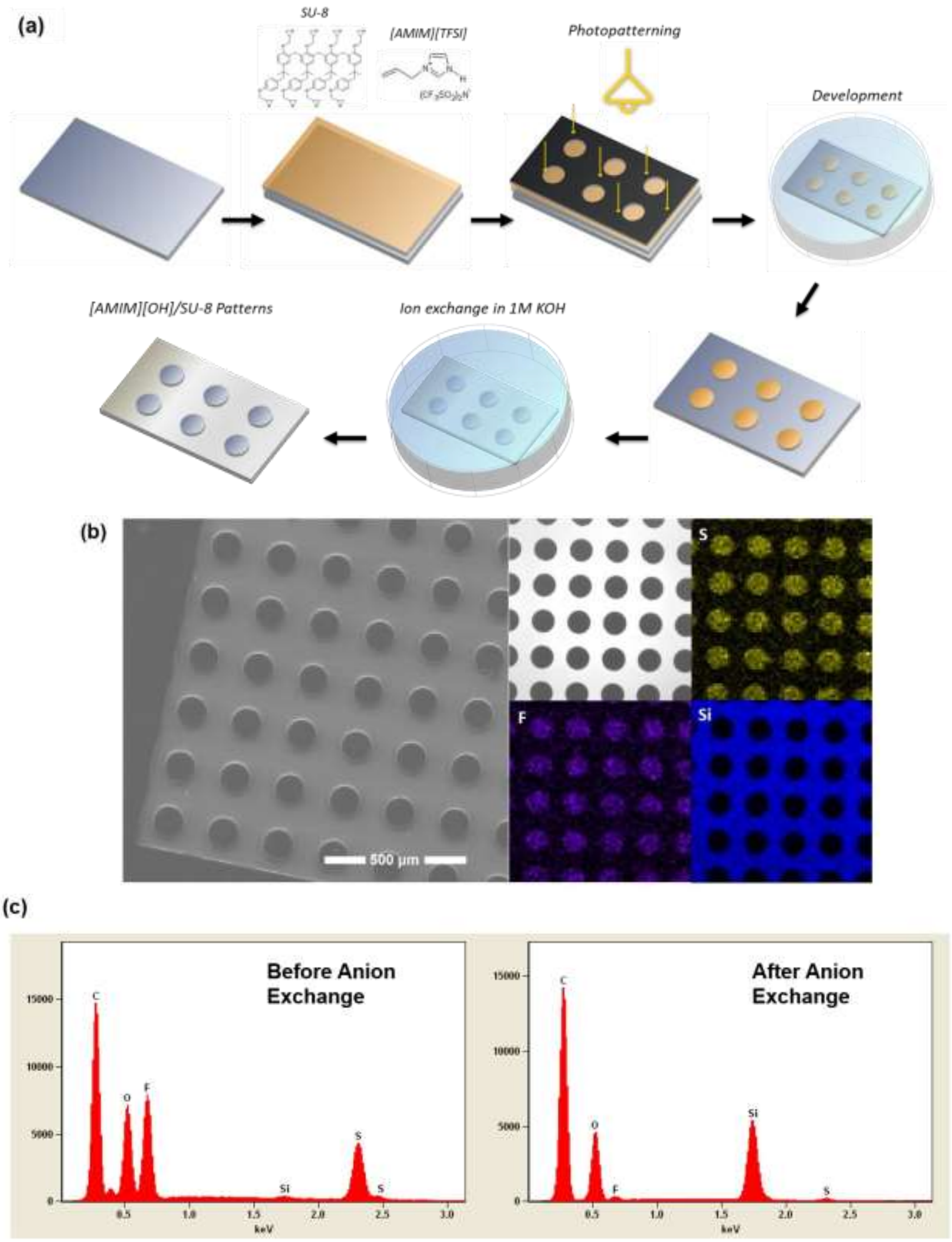
(a)
SU-8
[AMIM][TFSI]
(CF3SO2)2N-
Photopatterning
Development
[AMIM][OH]/SU-8 Patterns
Ion exchange in 1M KOH
(b)
500 µm
S
F
Si
(c)
Before Anion Exchange
After Anion Exchange
15000
10000
5000
0
C
O
F
Si
S
0.5
1.0
1.5
2.0
2.5
3.0
keV

Figure S1. (a) Schematic diagram of fabricating photopatternable [AMIM][OH] solid electrolytes. Epoxybased SU-8 photoresist was modified with the polymerizable ionic liquid and photopatterned using conventional photolithographic techniques. $TFSI^-$ anions in the photopatterns are then ion exchanged with hydroxides in aqueous KOH solution. (b) SEM images of photopatterned [AMIM][TFSI]/SU-8 electrolytes. Each circular feature represents 100 μm diameter cylindrical posts with 10 μm in height. EDS analysis of ionic liquid modified SU-8 electrolytes show the presence of sulfur and fluorine atoms, which come only from the [AMIM][TFSI], confirming the successful encapsulation of ionic liquids. (c) The EDS analysis of the photopatterned electrolyte monitoring sulfur and fluorine signals of $TFSI^-$ reveal that $TFSI^-$ anion has been successfully exchanged with hydroxides. After the anion exchange process, less than 1wt% trace amount of sulfur and fluorine were detected from the EDS analysis.

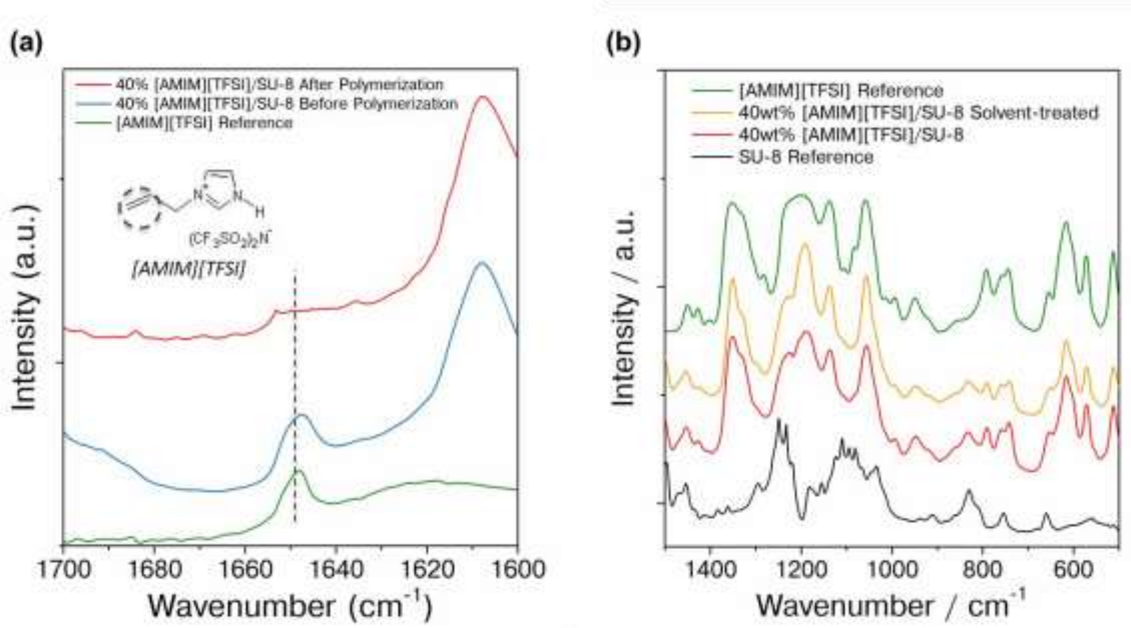

Figure S2. (a) FT-IR spectra of the [AMIM][TFSI] SU-8 before and after the polmyerization reaction and of neat [AMIM][TFSI] as a reference. The changes in the intensity of C=C group at 1648 cm^{-1} before and after polymerization indicate that the vinyl groups in the polymerizable ionic liquids have been fully reacted. The band at 1608 cm^{-1} is attributed to the aromatic ring of the SU-8 that does not undergo any chemical changes during the polymerization reaction. (b) FT-IR spectra of the [AMIM][TFSI] SU-8 and reference patterns. It shows that polymerized [AMIM][TFSI] in SU-8 is covalently bonded and not soluble in solvents.

Table S2. Characteristic IR absorption bands of [AMIM][TFSI] and their assignments

	Frequency (cm^{-1})	Dominant Vibrational assignment
Anion Assignment	569	CF_3 antisymmetric bend
	600	SO_2 antisymmetric bend
	611	SO_2 antisymmetric bend
	650	SNS bend
	789	CS stretch
	1051	SNS antisymmetric stretch
	1132	SO_2 symmetric stretch
	1182	CF_3 antisymmetric stretch
	1331	SO_2 antisymmetric stretch
	1348	SO_2 antisymmetric stretch
Cation	752	Ring HCCH symmetric bend

Assignment	1464	CCH HCH antisymmetric bend, CH_3(N)HCH symmetric bend, terminal CH_3 HCH antisymmetric bend
	1474	Ring in-plane antisymmetric stretch, CH_3(N) stretch

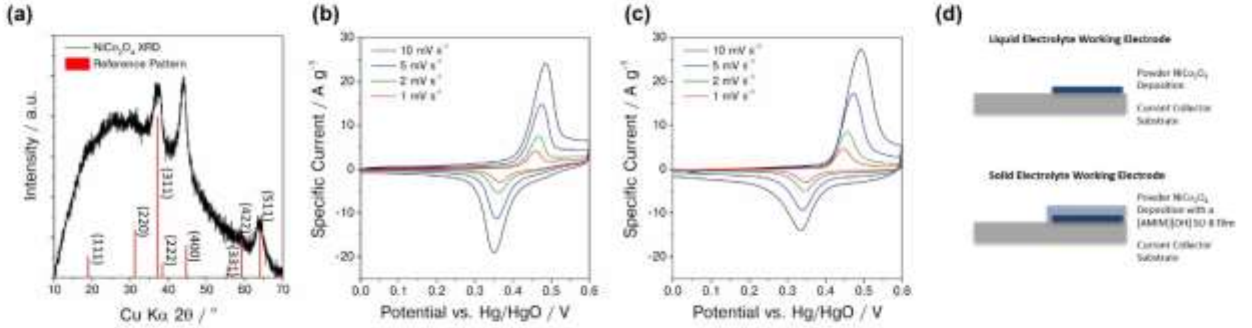

Figure S3. The nickel cobalt oxide material has been prepared by the microwave assisted synthesis. The corresponding XRD (a) shows low crystallinity of the material that did not affect the electrochemistry. CV curves of $NiCo_2O_4$ that were obtained using (b) OH^- conducting patternable electrolytes and (c) 1M KOH control liquid electrolytes. The redox behavior is similar in the two electrolytes, confirming that there is hydroxide conduction through the solid electrolyte. (d) Graphical diagram highlighting differences between the sample preparation of a solid-state working electrode versus a control electrode tested in liquid electrolytes.

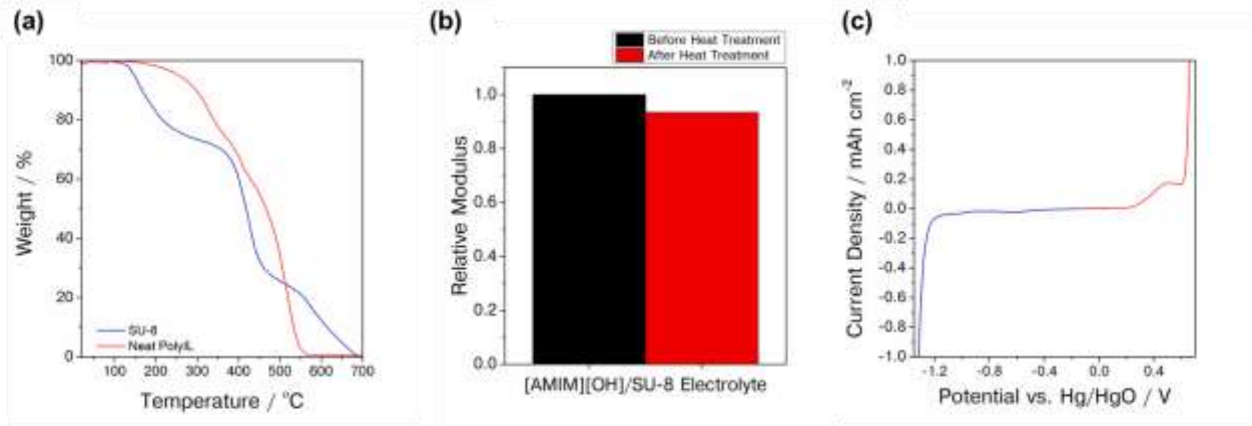

Figure S4. (a) TGA profile of neat [AMIM][TFSI] ionic liquid and SU-8. The thermal stability of [AMIM][OH] photopatternable electrolytes was significantly improved by incorporating thermally stable [AMIM][TFSI] ionic liquids. (b) Mechanical properties of [AMIM][OH]/SU-8 films measured by nanoindentation before and after heat treatment at 100°C for 12 hours. (c) Linear sweep voltammetry with [AMIM][OH]SU-8 electrolytes on a glassy carbon working electrode in three-electrode experiments. The photopatternable electrolyte was shown to have a decent electrochemical stability window with no residual current between -1.2 and 0.2 V (vs. Hg/HgO).

Physical and electrochemical properties of pseudocapacitive electrode materials

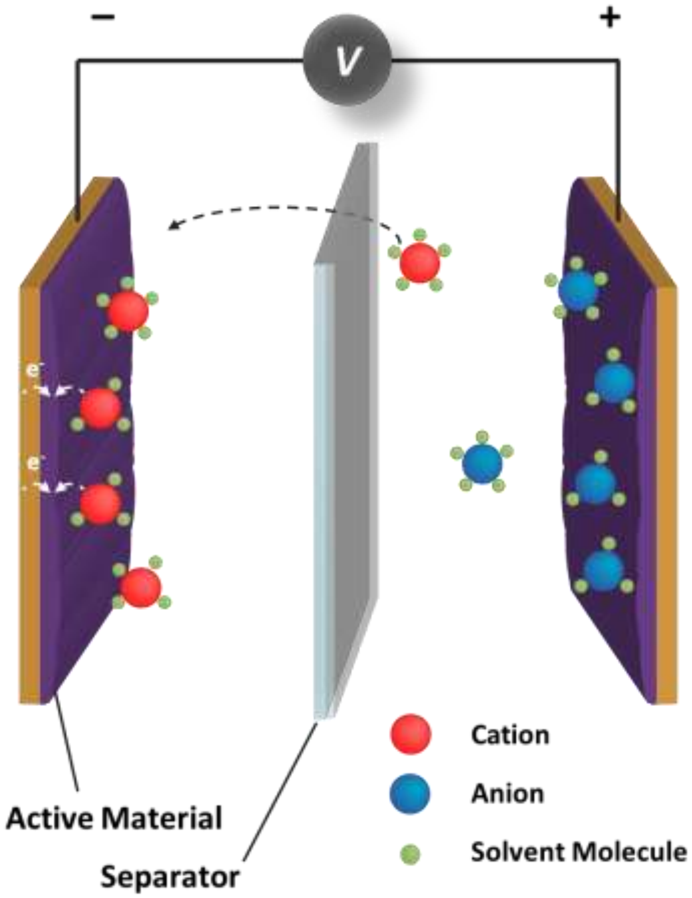

Figure S5. Schematic representation of a pseudocapacitive charge storage device. Pseudocapacitive materials such as RuO_2, MnO_2, and VN, store electrochemical energy primarily via a faradaic process involving surface or near-surface redox reactions. Due to this characteristic, pseudocapacitive materials exhibit capacitor-like electrochemical features.[12,13]

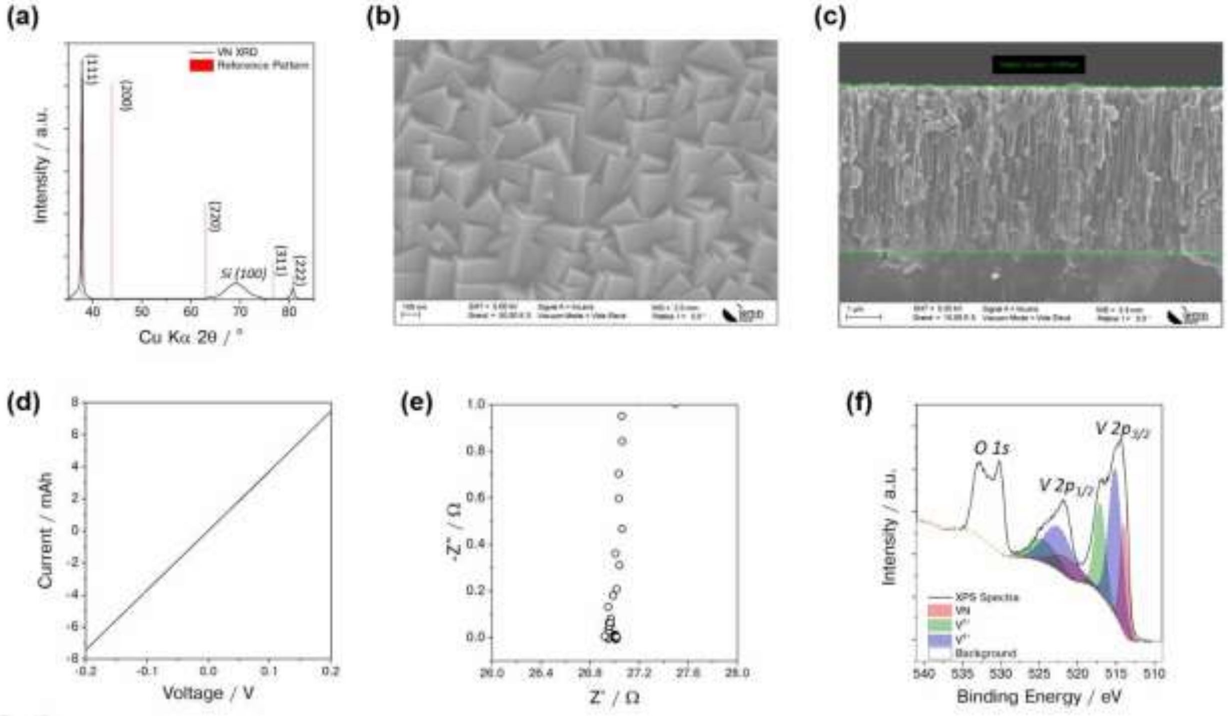

Figure S6. Chemical characterization of as-deposited VN films. (a) XRD patterns of the as-deposited VN show strong preferential orientation in (111) direction with visible (111) and (222) peaks. (b) Top down SEM image of the as-deposited VN. The grain growth of VN occurs in a strongly faceted manner. (c) Crosssectional SEM images of VN films, in which the intercolumnar structures can be observed. As-prepared VN thickness was about 5 μm. (d) The I–V curves of a VN film, exhibiting a linear I-V curve with the high electrical conductivity of 413 S cm^{-1}. (e) Nyquist impedance spectra of a VN film confirms the electrical conductivity measurement results obtained from the I-V curve. (f) XPS spectra (V 2p region) of the VN film. The V^{3+} and V^{4+} peaks ascribed vanadium oxynitride groups were present at the VN surface.

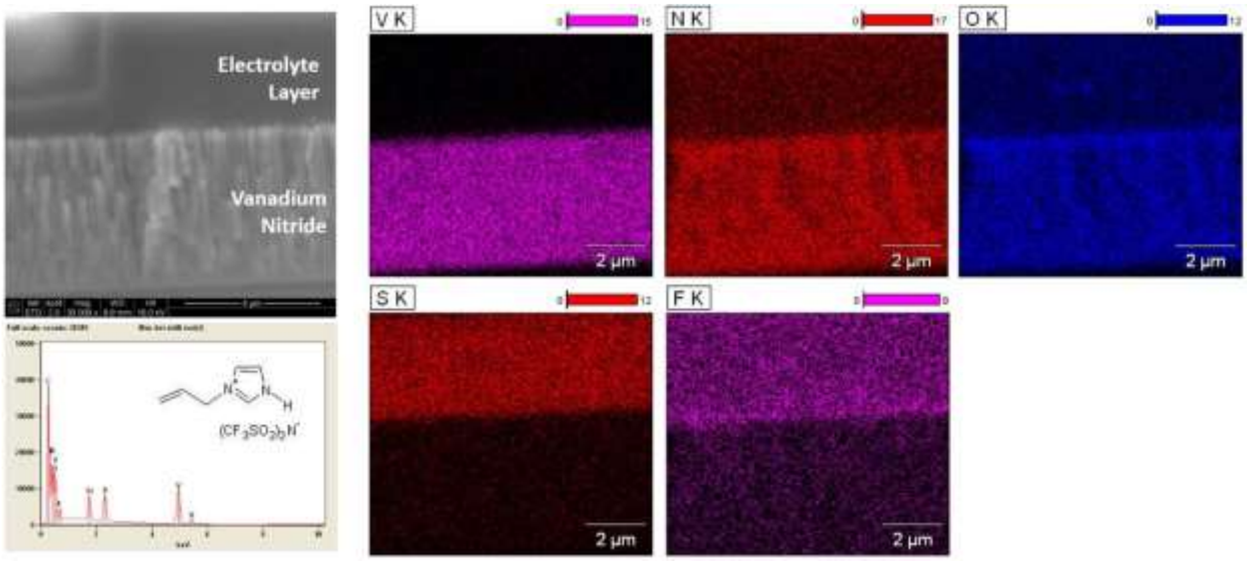

Figure S7. A cross-sectional SEM image of a planar VN electrode. The thickness of as-prepared VN was 5 μm and that of the solid electrolyte film was patterned to be 10 μm. EDS analysis of the solid electrolyte coated VN electrode verified the homogeneous distribution of sulfur and fluorine signals that are present in the [AMIM][TFSI] prior to the hydroxide anion exchange.

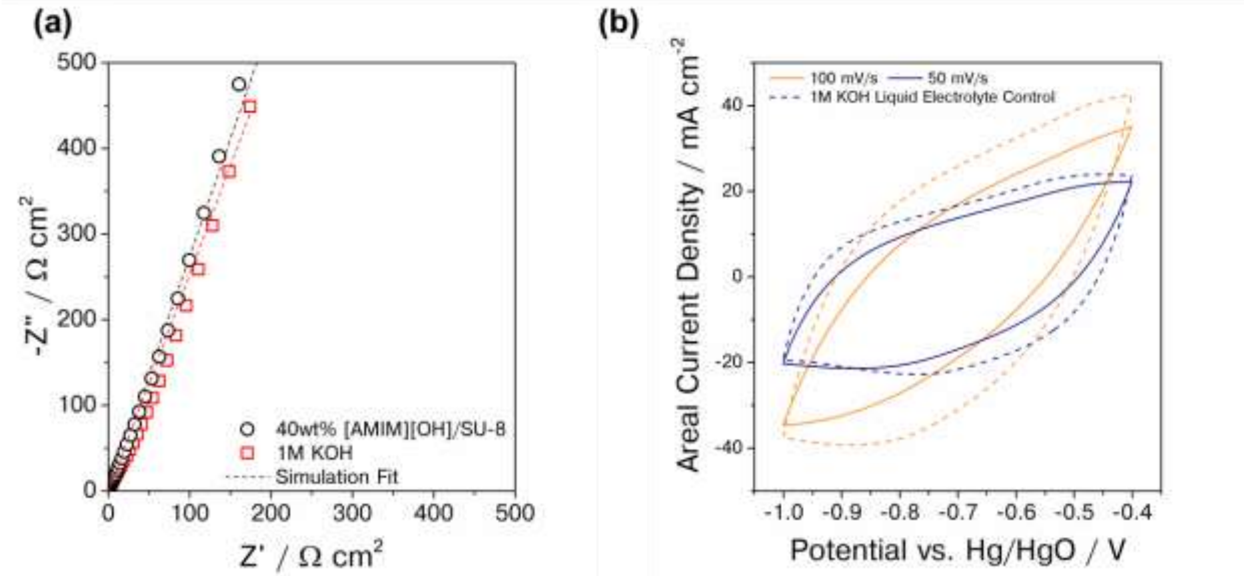

Figure S8. (a) Nyquist impedance spectra of [AMIM][OH] SU-8 and 1M KOH (zoom out of Figure 3a), demonstrating the capacitive tail at the low frequency region. (b) Cyclic voltammetry of the hydroxide photopatternable solid electrolyte patterned VN electrode at scan rates of 50 to 100 mV s^{-1}. The dashed lines represent the CV curve obtained from the 1M KOH liquid electrolyte which serves as a control.

Solid-state VN micro-supercapacitor fabrication

The central role played by the photopatternable hydroxide-conducting solid electrolyte in miniaturized EES applications is best shown by providing an overview of the vanadium nitride (VN) fabrication process in Figure S9a. Briefly, the vanadium nitride electrode material is sputtered onto a silicon (Si) / silicon nitride (Si_3N_4) substrate. An important benefit of VN-based MSC devices is that a separate current collector is not needed because of the high electronic conductivity for VN. The VN layer can then be patterned and selectively etched using conventional photolithography and plasma etching techniques, creating highresolution interdigitated electrodes with a minimum feature size of 10 µm. Subsequently, the liquid precursor for the solid-state electrolyte is spin-coated directly onto the interdigitated device structure to provide ion conduction between electrodes. The pseudocapacitive charge storage mechanism in VN involves a faradaic reaction between V^{4+} and V^{3+} through an oxy/oxyhydrate couple at the surface.[14] An important factor here is that the highest pseudocapacitive contributions to VN have been observed using basic electrolytes, with hydroxide being the dominant charge-carrying ion. This behavior indicates that fast ion transport of hydroxide in the solid electrolyte material is required in order to achieve rapid charge storage in VN materials.

The process was designed such that for each 3” wafer, 40 individual devices are fabricated and electrically connected in various series and parallel configurations without any additional metal layers. Each device has a 4 mm^2 footprint area and is composed of two VN interdigitated electrodes with a 10 µm spacing between electrode fingers. It is important to note that this spacing of 10 µm, the distance that charge carrying ions travel during charge/discharge, is much shorter than the thickness of commercial separators typically ranging between 20-50 µm.[15] The thickness of the VN layer is approximately 5 µm. Once interdigitated VN microdevices were fabricated, the hydroxide ion conducting solid electrolyte was patterned directly over, covering the entire device to provide ion conduction between the two VN electrodes upon charge/discharge.

Table S3. The important design parameters of wafer-scale fabrication of interdigitated MSC devices.

Number of interdigitated devices	**40**
Number of fingers per device	8.5
Finger length	2 mm
Finger width	100 µm
Space between fingers	10 µm
Active material (VN) loading	2.5 mg cm^{-2}
[AMIM][OH]/SU-8 Electrolyte loading	1.7 mg cm^{-2}
Gravimetric capacitance of the VN electrode	172 F/g

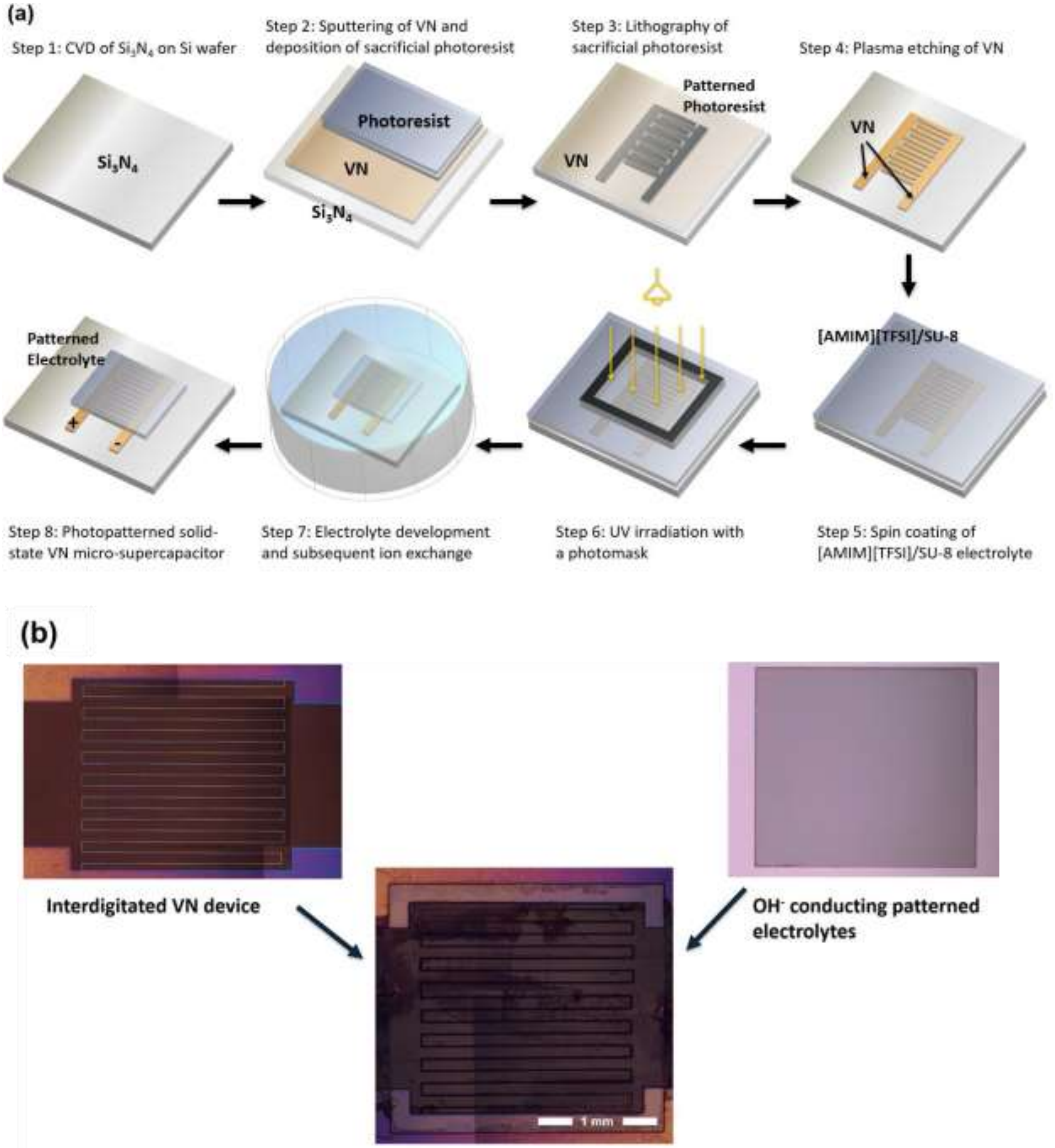

Figure S9. (a) Schematic representation of the process for fabricating solid-state VN MSCs using the photopatternable [AMIM][OH] electrolyte. Both electrode and electrolyte materials are formed through microfabrication techniques. (b) A fabrication approach to form solid-state MSC devices. Both electrode and electrolyte materials can be patterned to high-resolution features using microfabrication techniques.

Table S4. Comparison of interdigitated MSCs based on solid and liquid electrolytes

Solid Electrolyte

Electrode Materials	*Electrolyte Materials*	*Energy Density* [µWh/cm2] (Power Density in [mW/cm2])*	*Cycle Life (Retention)*	*Main Text Reference*
VN	[AMIM][OH]/SU-8	7.6 (9.1) 12.8 (0.8)	10,000 (80%)	This Work
MnO$_2$	[EMIM][TFSI]/PVDF	3.2 (3.8) 4.5 (0.7)	30,000 (96.2%)	19
Graphene	[BMIM][TFSI]/Fumed Silica	4.4 (45.4) 4.92 (0.4)	10,000 (96%)	43
Pyrolyzed Carbon	[EMIM][TFSI]/Fumed Silica	3.1 (3.1) 4.2 (0.8)	10,000 (94%)	44
MnO$_2$	LiCl/PVA	0.8 (3.8) 2.2 (0.6)	4,000 (92%)	45
RuO$_2$	H$_2$SO$_4$/PVA	0.6 (2.2) 3.3 (1.2)	10,000 (90%)	46

Liquid Electrolyte

Electrode Materials	*Electrolyte Materials*	*Energy Density [uWh/cm2] (Power Density in [mW/cm2])*	*Cycle Life (Retention)*	*Main Text Reference*
VN	1M KOH	10.6 (0.2) 0.9 (4.1)	50,000 (80%)	9
CDC	1M H$_2$SO$_4$	1.6 (0.3) 1.2 (8.9)	10,000 (100%)	7

* Energy density at a given power density. Power density is in parentheses. Energy density given at low and high values of power density.

Supporting Information References:

1. Yan, J., Li, S., Lan, B., Wu, Y., and Lee, P.S. (2020). Rational Design of Nanostructured Electrode Materials toward Multifunctional Supercapacitors. Adv. Funct. Mater. *30*, 1902564.

2. Zhao, J., Lu, H., Zhao, X., Malyi, O.I., Peng, J., Lu, C., Li, X., Zhang, Y., Zeng, Z., Xing, G., et al. (2020). Printable Ink Design towards Customizable Miniaturized Energy Storage Devices. ACS Materials Lett. *2*, 1041–1056.

3. Chen, D., Jiang, K., Huang, T., and Shen, G. (2020). Recent Advances in Fiber Supercapacitors: Materials, Device Configurations, and Applications. Adv. Mater. *32*, 1901806.

4. Hota, M.K., Jiang, Q., Wang, Z., Wang, Z.L., Salama, K.N., and Alshareef, H.N. (2019). Integration of Electrochemical Microsupercapacitors with Thin Film Electronics for On Chip Energy Storage. Adv. Mater. *31*, 1807450.

5. Eustache, E., Douard, C., Demortière, A., De Andrade, V., Brachet, M., Le Bideau, J., Brousse, T., and Lethien, C. (2017). High Areal Energy 3D-Interdigitated Micro-Supercapacitors in Aqueous and Ionic Liquid Electrolytes. Adv. Mater. Technol. *2*, 1700126.

6. Orangi, J., Hamade, F., Davis, V.A., and Beidaghi, M. (2020). 3D Printing of Additive-Free 2D Ti $_3$ C $_2$ T $_x$ (MXene) Ink for Fabrication of Micro-Supercapacitors with Ultra-High Energy Densities. ACS Nano *14*, 640–650.

7. Yang, W., Yang, J., Byun, J.J., Moissinac, F.P., Xu, J., Haigh, S.J., Domingos, M., Bissett, M.A., Dryfe, R.A.W., and Barg, S. (2019). 3D Printing of Freestanding MXene Architectures for Current Collector Free Supercapacitors. Adv. Mater. *31*, 1902725.

8. Lamberti, A., Clerici, F., Fontana, M., and Scaltrito, L. (2016). A Highly Stretchable Supercapacitor Using Laser-Induced Graphene Electrodes onto Elastomeric Substrate. Adv. Energy Mater. *6*, 1600050.

9. Cao, D., Xing, Y., Tantratian, K., Wang, X., Ma, Y., Mukhopadhyay, A., Cheng, Z., Zhang, Q., Jiao, Y., Chen, L., et al. (2019). 3D Printed High Performance Lithium Metal Microbatteries Enabled by Nanocellulose. Adv. Mater. *31*, 1807313.

10. Wang, Y., Chen, C., Xie, H., Gao, T., Yao, Y., Pastel, G., Han, X., Li, Y., Zhao, J., Fu, K.K., et al. (2017). 3D-Printed All-Fiber Li-Ion Battery toward Wearable Energy Storage. Adv. Funct. Mater. *27*, 1703140.

11. Zhao, J., Lu, H., Zhang, Y., Yu, S., Malyi, O.I., Zhao, X., Wang, L., Wang, H., Peng, J., Li, X., et al. (2021). Direct coherent multi-ink printing of fabric supercapacitors. Sci. Adv. *7*, eabd6978.

12. Choi, C., Ashby, D.S., Butts, D.M., DeBlock, R.H., Wei, Q., Lau, J., and Dunn, B. (2020). Achieving high energy density and high power density with pseudocapacitive materials. Nat Rev Mater *5*, 5–19.

13. Augustyn, V., Simon, P., and Dunn, B. (2014). Pseudocapacitive oxide materials for high-rate electrochemical energy storage. Energy & Environmental Science *7*, 1597.

14. Robert, K., Stiévenard, D., Deresmes, D., Douard, C., Iadecola, A., Troadec, D., Simon, P., Nuns, N., Marinova, M., Huvé, M., et al. (2020). Novel insights into the charge storage mechanism in pseudocapacitive vanadium nitride thick films for high-performance on-chip micro-supercapacitors. Energy Environ. Sci. *13*, 949–957.

15. Lagadec, M.F., Zahn, R., and Wood, V. (2019). Characterization and performance evaluation of lithium-ion battery separators. Nat Energy *4*, 16–25.